

See discussions, stats, and author profiles for this publication at: <https://www.researchgate.net/publication/263131310>

# Three-Dimensional Thin Film for Lithium-Ion Batteries and Supercapacitors

ARTICLE *in* ACS NANO · JUNE 2014

Impact Factor: 12.88 · DOI: 10.1021/nn502341x · Source: PubMed

CITATIONS

12

READS

54

9 AUTHORS, INCLUDING:



**Yang Yang**

Rice University

43 PUBLICATIONS 630 CITATIONS

SEE PROFILE



**Zhiwei Peng**

University of Maryland, College Park

49 PUBLICATIONS 1,460 CITATIONS

SEE PROFILE



**Gunuk Wang**

Korea University

61 PUBLICATIONS 1,177 CITATIONS

SEE PROFILE



**Lei Li**

New York State Department of Health

32 PUBLICATIONS 610 CITATIONS

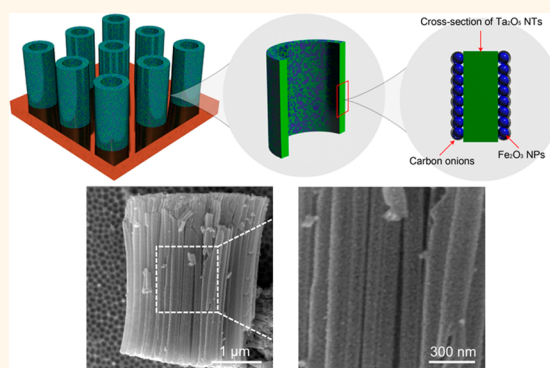
SEE PROFILE

# Three-Dimensional Thin Film for Lithium-Ion Batteries and Supercapacitors

Yang Yang,<sup>†,‡,§</sup> Zhiwei Peng,<sup>†,§</sup> Gunuk Wang,<sup>†,‡</sup> Gedeng Ruan,<sup>†</sup> Xiujuan Fan,<sup>‡,||</sup> Lei Li,<sup>†</sup> Huilong Fei,<sup>†</sup> Robert H. Hauge,<sup>†,‡,⊥</sup> and James M. Tour<sup>†,‡,§,\*</sup>

<sup>†</sup>Department of Chemistry, <sup>‡</sup>Smalley Institute for Nanoscale Science and Technology, and <sup>§</sup>Department of Materials Science and NanoEngineering, Rice University, 6100 Main Street, Houston, Texas 77005, United States, <sup>||</sup>College of Electronic Information and Control Engineering, Beijing University of Technology, Beijing, 100124, China, and <sup>⊥</sup>King Abdulaziz University, P.O. Box 80203, Jeddah 21589, Saudi Arabia. <sup>#</sup>Y.Y. and Z.P. contributed equally to this work.

**ABSTRACT** Three-dimensional heterogeneously nanostructured thin-film electrodes were fabricated by using Ta<sub>2</sub>O<sub>5</sub> nanotubes as a framework to support carbon-onion-coated Fe<sub>2</sub>O<sub>3</sub> nanoparticles along the surface of the nanotubes. Carbon onion layers function as microelectrodes to separate the two different metal oxides and form a nanoscale 3-D sandwich structure. In this way, space-charge layers were formed at the phase boundaries, and it provides additional energy storage by charge separation. These 3-D nanostructured thin films deliver both excellent Li-ion battery properties (stabilized at 800 mAh cm<sup>-3</sup>) and supercapacitor (up to 18.2 mF cm<sup>-2</sup>) performance owing to the synergistic effects of the heterogeneous structure. Thus, Li-ion batteries and supercapacitors are successfully assembled into the same electrode, which is promising for next generation hybrid energy storage and delivery devices.



**KEYWORDS:** heterogeneous structure · nanotube · lithium-ion battery · supercapacitor · multifunctional

Electrochemical energy storage devices such as Li-ion batteries (LIBs) and electrochemical supercapacitors (ECs) are the most popular power supplies in portable electronic devices (PEDs),<sup>1,2</sup> and intense ongoing research seeks to develop hybrid energy devices and multifunctional electrodes that combine the advantages of LIBs (high energy density and capacity) and ECs (high power density and long-term cyclability) within micro- or lower dimensions.<sup>3</sup> Until now, carbon materials such as carbon nanotubes and graphene nanoribbons have been widely used either directly for LIB anodes and ECs or as conductive network components in composites.<sup>4,5</sup> However, the low charge storage capability of carbon materials (theoretically 372 mAh g<sup>-1</sup> in LIB anodes and <150 F g<sup>-1</sup> in ECs) limits their further applications in energy storage. Therefore, transition metal oxides,<sup>6</sup> especially Fe<sub>2</sub>O<sub>3</sub>, which is known for its high theoretical charge storage capability (1005 mA h g<sup>-1</sup> in LIB anodes and 1342 F g<sup>-1</sup> in ECs) and natural

abundance,<sup>7</sup> have been developed as attractive electrode materials. However, the severe volume change during charge/discharge cycles and the initial capacity loss (ICL) restrict the further application of nanostructured Fe<sub>2</sub>O<sub>3</sub> as a LIB anode.<sup>8,9</sup> Furthermore, most of the transition metal oxides have low electronic conductivity retarding their use in electrochemical energy storage.<sup>10</sup> One way to confine the volume change of Fe<sub>2</sub>O<sub>3</sub> and enhance the electronic conductivity of the electrode is to form passivation shells of carbon onions (few-layer graphene or graphitic shells) by chemical vapor deposition (CVD).<sup>11,12</sup>

Nanosized materials (generally powders) can improve electrochemical performance by forming abundant electrochemically active sites; however, without excellent dispersion or loading on supporting materials, side effects such as higher contact resistance due to agglomeration will have a negative impact on their energy storage performance.<sup>13,14</sup> Moreover, the conventional fabrication

\* Address correspondence to tour@rice.edu.

Received for review April 29, 2014  
and accepted June 15, 2014.

Published online  
10.1021/nn502341x

© XXXX American Chemical Society

processes (mixing with additives such as binder and conductive carbon and then compressing the composite on the current collector to form an electrode film) could lessen the advantages of those nanoscale powders.<sup>15</sup> Thus, self-organized nanostructured films, especially nanotubes (NTs) *in situ* grown on conductive substrates with facilitated ion transportation in their three-dimensional (3-D) open frameworks, could be used as active support materials for energy storage.<sup>16,17</sup> This further reduces the weight of the electrodes.<sup>18</sup> After nanoparticles (NPs) are anchored on the surface of nanotubes to form a hybrid nanostructure,<sup>19</sup> more electrochemically active sites are expected, along with synergistic effects from the heterogeneous phase boundaries. In this work, Ta<sub>2</sub>O<sub>5</sub> NTs were selected as active support materials with good thermal stability that can be used for catalytic graphene growth at high temperature (850 °C) without breaking the nanotubular structure.<sup>20,21</sup> Carbon-onion-coated Fe<sub>2</sub>O<sub>3</sub> NPs (C-Fe<sub>2</sub>O<sub>3</sub> NPs) are then uniformly coated along the Ta<sub>2</sub>O<sub>5</sub> NTs to deliver multifunctional energy storage by combining LIB and supercapacitor performance

into the same electrode material. The work described here puts forward a concept that can solve problems in designing battery–supercapacitor hybrid energy storage systems through the development of new nanostructured bifunctional electrode materials.<sup>22</sup>

## RESULTS AND DISCUSSION

In a first approach, Ta<sub>2</sub>O<sub>5</sub> nanotubes that were 100–150 nm in diameter and 3.5  $\mu$ m in length were obtained by anodization treatment on tantalum foils. These were used as a matrix to uniformly anchor iron oxide NPs along the channels of the NTs. Reduction of the iron oxide to metallic iron followed by CVD growth of carbon onions on the iron catalysts afforded the requisite framework. A postannealing was performed on the samples to convert the metallic iron (used as a catalyst for the CVD graphene growth) back to electrochemically active Fe<sub>2</sub>O<sub>3</sub>. A morphology change from the smooth surface before anchoring of the C-Fe<sub>2</sub>O<sub>3</sub> NPs (Supporting Information Figure S1a,b) to a roughened surface after anchoring the C-Fe<sub>2</sub>O<sub>3</sub> NPs (Figure 1) exemplifies the uniform anchoring of C-Fe<sub>2</sub>O<sub>3</sub> NPs on

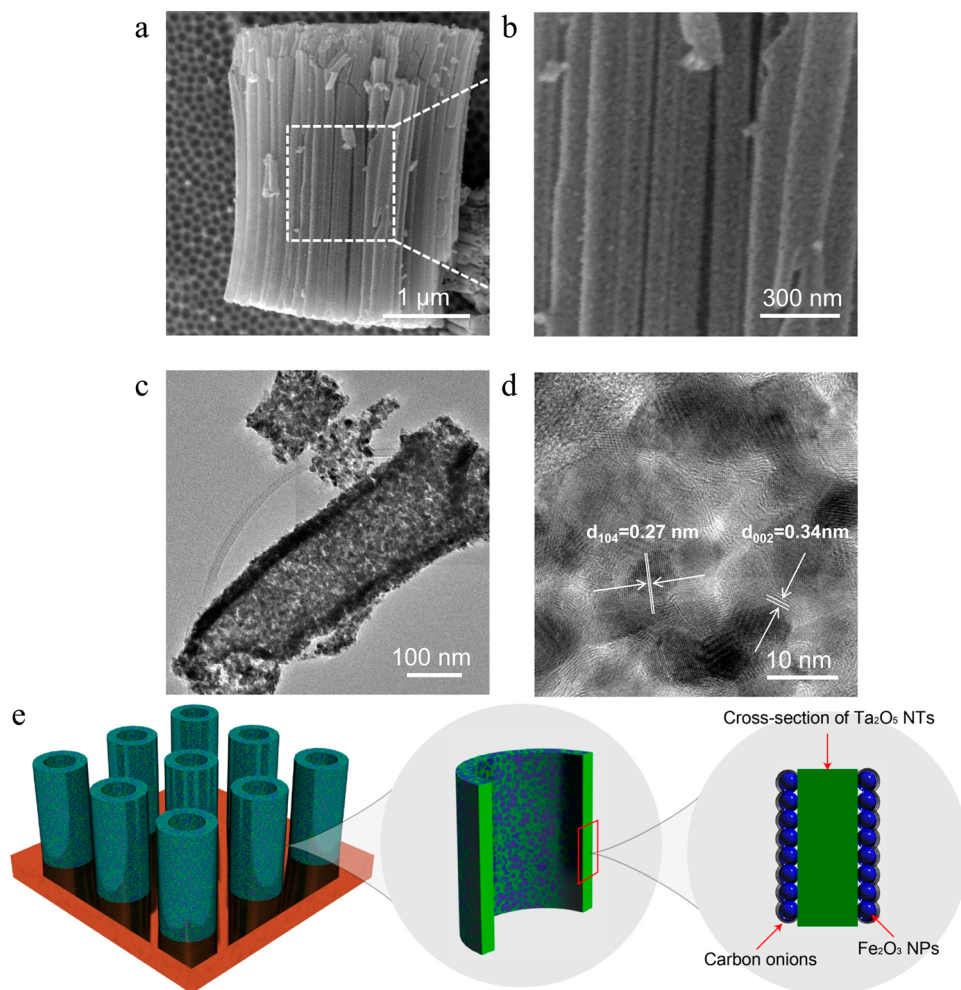


**Figure 1.** Microscopy observation of the heterogeneous nanotubes. (a,b) SEM images of Ta<sub>2</sub>O<sub>5</sub> NTs covered with C-Fe<sub>2</sub>O<sub>3</sub> NPs. (c) Cross-sectional TEM image of the heterogeneous nanotubes. (d) HRTEM image of the C-Fe<sub>2</sub>O<sub>3</sub> NPs. (e) Schematic figure for the Ta<sub>2</sub>O<sub>5</sub> NTs coated with C-Fe<sub>2</sub>O<sub>3</sub> NPs.

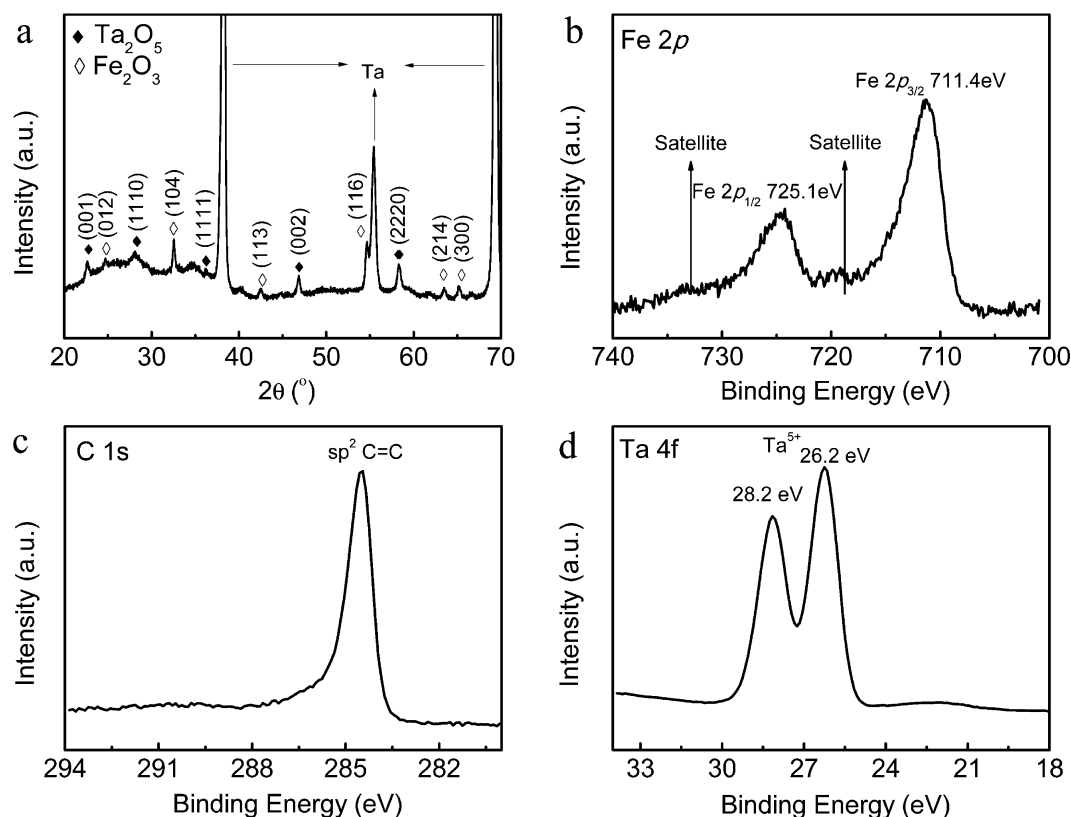


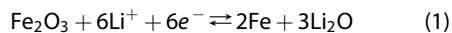
**Figure 2.** Crystallinity and chemical composition analysis of the heterogeneous nanotubes. (a) XRD pattern. (b–d) XPS Fe 2p, C 1s, and Ta 4f spectra, respectively.

the surface of the undamaged Ta<sub>2</sub>O<sub>5</sub> NTs (schematic picture is shown in Figure 1e). The uniform Fe<sub>2</sub>O<sub>3</sub> NPs coating on both sides of Ta<sub>2</sub>O<sub>5</sub> NTs does not block the open channels as can be determined by examination of the cross-sectional and top-view SEM images (Supporting Information Figure S1c,d). It is also apparent from transmission electron microscopy (TEM) observation (Figure 1c and Supporting Information Figure S2) that the C-Fe<sub>2</sub>O<sub>3</sub> NPs were uniformly anchored on Ta<sub>2</sub>O<sub>5</sub> NTs without agglomeration of the nanoparticles or blocking the channels of the nanotubes. C-Fe<sub>2</sub>O<sub>3</sub> NPs with average size of 5–10 nm coated with 6–8-layer graphene (carbon onions) were identified by the *d*-spacing, of 0.27 and 0.34, respectively, from the lattice fringes observed by high-resolution TEM (HRTEM, Figure 1d and Supporting Information Figure S3).

The crystalline structure and chemical composition were investigated by X-ray diffraction (XRD) and X-ray photoelectron spectroscopy (XPS). Crystalline Fe<sub>2</sub>O<sub>3</sub> (PDF 00-033-0664) and Ta<sub>2</sub>O<sub>5</sub> (PDF 00-018-1304) were identified from the XRD patterns (Figure 2a), whereas only Ta, Fe, C, and O were identified from the XPS spectra (Figure 2b–d and Supporting Information Figure S4). From the XPS Fe 2p spectrum, Fe 2p<sub>1/2</sub> and Fe 2p<sub>3/2</sub> peaks at 725.1 and 711.4 eV can be assigned to Fe<sup>3+</sup>, which confirm the formation of Fe<sub>2</sub>O<sub>3</sub> instead of Fe<sub>3</sub>O<sub>4</sub>.<sup>23</sup> Furthermore, the peaks at 26.2 and 28.2 eV in the XPS Ta 4f spectrum are attributed to the higher oxidation state

of Ta<sup>5+</sup> in Ta<sub>2</sub>O<sub>5</sub>.<sup>24</sup> The typical sp<sup>2</sup> C=C bonding is from the carbon onions, which have a graphitic structure.<sup>25</sup> The content of each component, C, Fe<sub>2</sub>O<sub>3</sub>, and Ta<sub>2</sub>O<sub>5</sub>, in the hybrid nanotubes, estimated semiquantitatively from XPS, is 27, 13, and 60 wt %, respectively.

Cyclic voltammetry (CV) was performed on the samples within a potential window between 0.01 and 3 V (vs Li/Li<sup>+</sup>) at a scan rate of 0.5 mV s<sup>−1</sup> to access the electrochemical reactions that occurred during the initial two lithium insertion/extraction cycles (Figure 3a). Control experiments were also conducted to investigate the LIB performance of the heterogeneous nanotubes: (1) control-1, Ta<sub>2</sub>O<sub>5</sub> NTs without sensitizer (#C-1); (2) control-2, C-Fe<sub>2</sub>O<sub>3</sub> deposited on tantalum foils (#C-2). All the samples including control experiments were treated using the same procedure. Considering that a defined nanostructure was integrated into thin films, the performance evaluation in this work is based on the volume and area of the thin film (the nanotubes only without considering the Ta substrates). From the voltammograms of #C-2 (inset in Figure 3a), a cathodic peak at 0.79 V and an anodic peak at 1.62 V were assigned to the lithium insertion/extraction reactions that are shown in eq 1:<sup>26</sup>



and from voltammograms of #C-1, the redox peaks located at 0.69 (cathodic) and 1.21 V (anodic) reflect

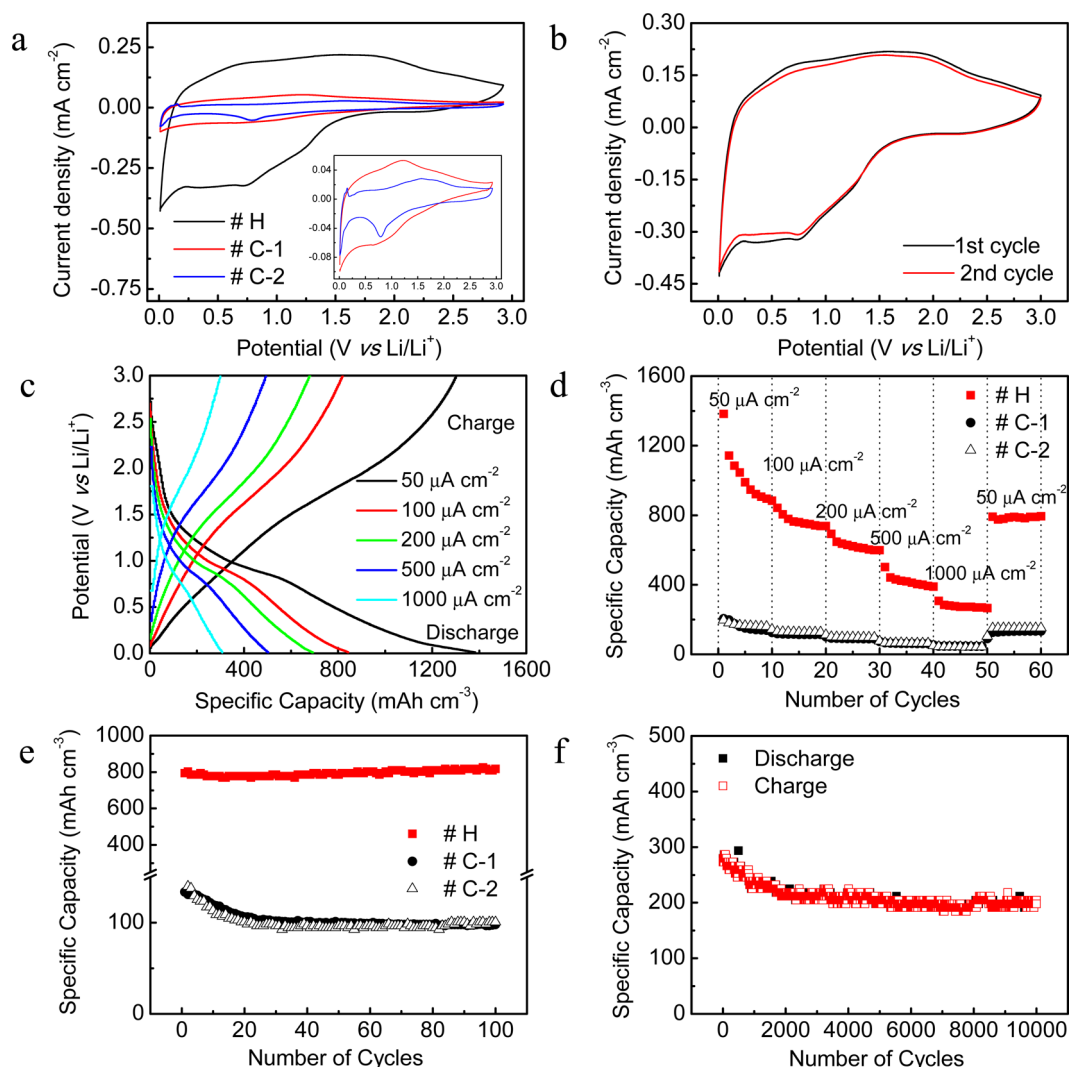
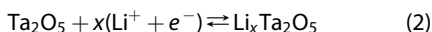


**Figure 3.** Electrochemical performance of the heterogeneous nanotubes (denoted by #H in the figures) for Li-ion batteries. (a) CV was performed over a potential window between 0.01 and 3 V (vs Li/Li<sup>+</sup>) at a scan rate of 0.5 mV s<sup>-1</sup>. The voltammograms of control experiments are shown in the inset. (b) Initial two voltammograms from the heterogeneous nanotubes at 0.5 mV s<sup>-1</sup>. (c,d) Galvanostatic discharge/charge curves and rate capacity obtained at different applied current densities from 50 to 1000 μA cm<sup>-2</sup>, respectively. (e,f) Cycling tests measured at 50 μA cm<sup>-2</sup> for 100 cycles and 1000 μA cm<sup>-2</sup> for 10 000 cycles with Coulombic efficiency higher than 97%.

the reversible Li-ion insertion/extraction and the phase transition between Ta<sub>2</sub>O<sub>5</sub> and Ta suboxides such as TaO<sub>2</sub>, TaO, and Ta<sub>2</sub>O as in eq 2:<sup>27</sup>



whereas voltammograms of the heterogeneous nanotubes show combined redox peaks that indicate multiple reactions of both Ta<sub>2</sub>O<sub>5</sub> and Fe<sub>2</sub>O<sub>3</sub> with lithium. By comparing the first and second voltammograms of the heterogeneous nanotubes (Figure 3b), no redox peak shifts were detected and only a slight peak current decrease could be distinguished, which indicates that suppression of most electrolyte decomposition was achieved.

Galvanostatic discharge/charge tests were performed on the samples at current densities from 50 to 1000 μA cm<sup>-2</sup> (Figure 3c) to investigate their lithium

insertion/extraction reactions. The discharge pseudo-plateau at ~0.9 V and the slope from ~1.4 to 2 V in charge are attributed to the lithium insertion/extraction reactions with Fe<sub>2</sub>O<sub>3</sub> due to the distinctive two-phase (lithium-poor phase, Fe, and lithium-rich phase, Li<sub>2</sub>O) coexistence characteristics.<sup>26</sup> With continuous increase in the applied current density, the potentials for lithium insertion/extraction reactions undergo no noticeable changes. From the discharge/charge profiles of #C-1 (Supporting Information Figure S5a), no obvious lithium insertion/extraction plateau was detected due to the solid solution reactions of Ta<sub>2</sub>O<sub>5</sub> with lithium instead of the desired two-phase equilibrium. A more prominent discharge plateau at 0.75 V is distinguished from #C-2 (Supporting Information Figure S5b), which indicates that a new phase was formed that reached two-phase equilibrium during the lithium insertion reaction.



However, the discharge plateau shifts to 0.9 V after the first discharge/charge cycle because of irreversible reactions occurring in the first discharge such as severe decomposition of electrolyte and the formation of the solid-electrolyte-interface (SEI) film.<sup>8</sup> Such irreversible reactions consume a large amount of lithium in the electrolyte and change the equilibrium potential of the cell, which are the origins of large ICL and poor cyclability. From the rate capacity tests (Figure 3d), a gradually stabilized capacity from 1400 to 800 mAh cm<sup>-3</sup> at a current density of 50  $\mu$ A cm<sup>-2</sup> was observed from the first few cycles in the heterogeneous nanotubes due to the buffered electrolyte decomposition. The stable capacity (800 mAh cm<sup>-3</sup>) obtained is even higher than that found in most 3-D electrodes.<sup>28–30</sup> With an increase in the applied current up to 1000  $\mu$ A cm<sup>-2</sup>, a capacity of 280 mAh cm<sup>-3</sup> is maintained (35% retention), which is still appealing for high power energy storage. When the current density was reduced to 50  $\mu$ A cm<sup>-2</sup>, a capacity of 800 mAh cm<sup>-3</sup> was recovered without any polarization effect. The synergism effect between C-Fe<sub>2</sub>O<sub>3</sub> NPs and Ta<sub>2</sub>O<sub>5</sub> NTs in these heterogeneous nanostructured thin-film anodes delivers higher capacity at different current densities than in each material by itself. This is probably due to the additional lithium storage provided by the charge separation at the space-charge layers formed in the heterogeneous structure (two-phase boundaries).<sup>31,32</sup>

To investigate the long-term cycling stability of the heterogeneous nanotubes, cyclability tests at 50 and 1000  $\mu$ A cm<sup>-2</sup> were performed on the samples for 100 and 10 000 continuous cycles after the C rate tests (Figure 3e,f). It is evident that the heterogeneous nanotubes show stable capacity of 800 mAh cm<sup>-3</sup> for 100 cycles while the control samples show continuous capacity decay in the initial 20 cycles. Additionally, the high rate capacity of the heterogeneous nanotubes can be stabilized at 200 mAh cm<sup>-3</sup> for 10 000 cycles, which confirms the electrochemically stable characteristic of the heterogeneous structure. After cyclability tests, the heterogeneous nanotubes were disassembled from the coin cell and cleaned with dimethyl carbonate and acetone for scanning electron microscopy (SEM) observation. The heterogeneous nanotubes maintained their ordered nanotubular structure (Supporting Information Figure S6) without losing the anchored C-Fe<sub>2</sub>O<sub>3</sub> NPs after cycling.

Electrochemical impedance spectroscopy (EIS) is used to study the electrode kinetics of lithium insertion/extraction reactions. Nyquist plots (Supporting Information Figure S7a,b) for the samples were measured at open circuit potential (OCP) to investigate their kinetics. The correspondence between frequency-dependent impedance and equivalent circuit elements are illustrated in Figure S7a. The internal resistance of the cell ( $R_s$ ), starting from an intercept with the real axis, reflects

the combined resistance of the electrolyte, separator, and electrodes. Subsequently, the semicircle observed in the high-to-medium frequency region was due to either resistance induced by lithium migration through the SEI film ( $R_{SEI}$ ), associated with a SEI film capacitance (constant phase element, CPE<sub>SEI</sub>) at high frequency, or the charge-transfer resistance ( $R_{ct}$ ) and double-layer capacitance (CPE<sub>dl</sub>) at medium frequency. A sloping line at the low-frequency end is regarded as the Warburg impedance ( $Z_w$ ), representing solid-state diffusion of lithium through the electrode–electrolyte interface, followed by intercalation capacitance ( $C_{int}$ ). Due to the Faradaic characteristics of  $R_{ct}$  and  $Z_w$ , it is of special importance to investigate the electrochemical kinetics of the electrodes by monitoring the value change in  $R_{ct}$  and  $Z_w$  during lithium insertion/extraction reactions. After the Nyquist plots were fitted (Figure S7b),  $R_{ct}$  is reduced from 452.8  $\pm$  15.2  $\Omega$  (#C-1) and 455.4  $\pm$  3.5  $\Omega$  (#C-2) to 225.2  $\pm$  6.7  $\Omega$  (heterogeneous nanotubes) and  $Z_w$  is reduced from 61.9  $\pm$  17.8  $\Omega$  (#C-1) and 73.9  $\pm$  12.3  $\Omega$  (#C-2) to 51.9  $\pm$  2.5  $\Omega$  (heterogeneous nanotubes). The obviously reduced  $R_{ct}$  indicates that the greatly improved kinetics for Faradaic reactions of lithium insertion/extraction is obtained. To further demonstrate the electrode kinetics during lithium insertion/extraction reactions, EIS was measured during discharge/charge cycling (Supporting Information Figure S8). From the variations of  $R_{ct}$  and  $Z_w$  measured at electrode potentials (Supporting Information Figure S7c,d), it is apparent that both  $R_{ct}$  and  $Z_w$  of the heterogeneous nanotubes are substantially reduced compared to control samples throughout the discharge/charge cycling, which indicates a greatly enhanced charge transfer in the redox reactions on the surface of electrodes and improved lithium solid diffusion kinetics in the electrodes. Furthermore, the heterogeneous nanotubes in this work present particular structural advantages over most recently developed and commercial 3-D thin-film batteries: (1) highly ordered nanotubular structure serves as a stable host to anchor C-Fe<sub>2</sub>O<sub>3</sub> NPs without losing the advantages of nanoscale size effects caused by agglomeration; (2) two-phase boundaries between heterogeneous oxides provide a synergistic effect with additional charge separation at phase boundaries. Principally, the greatly enhanced LIB performance of the heterogeneous nanotubes is from the mutual benefits between the dual host Ta<sub>2</sub>O<sub>5</sub> NTs and C-Fe<sub>2</sub>O<sub>3</sub> NPs.

Based on the interesting nanostructure of the 3-D heterogeneous nanotubes (see schematic picture in Figure 1e), C-Fe<sub>2</sub>O<sub>3</sub>-treated Ta<sub>2</sub>O<sub>5</sub> NTs developed in this work could also be used for supercapacitors due to its ordered microsandwich structure (two C-Fe<sub>2</sub>O<sub>3</sub> NPs layers sandwiching a Ta<sub>2</sub>O<sub>5</sub> NT layer). Supercapacitive performance was tested first by CV at different scan rates from 10 mV s<sup>-1</sup> to 10 V s<sup>-1</sup> in two-electrode symmetric coin cells. The measured voltammograms (Figure 4a,b) show rectangular or quasi-rectangular

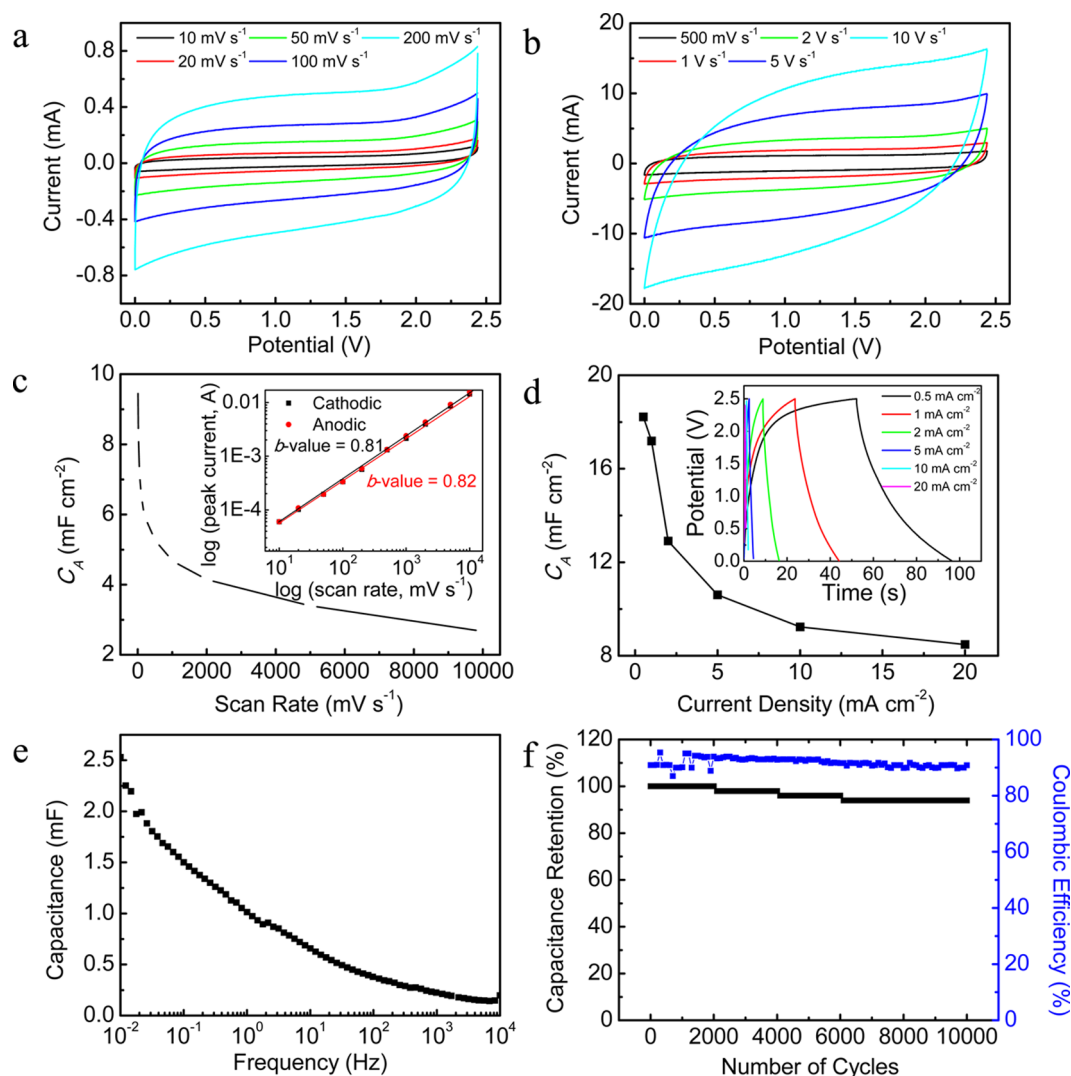


**Figure 4.** Electrochemical performance of the heterogeneous nanotubes for symmetrical supercapacitors. (a) CV performed over a potential window between 0 and 2.5 V at scan rates from 10 to 200  $\text{mV s}^{-1}$ . (b) CV performed over a potential window between 0 and 2.5 V at scan rates from 500  $\text{mV s}^{-1}$  to 10  $\text{V s}^{-1}$ . (c) Variation of areal capacitance at different scan rates. A log–log plot for the heterogeneous nanotubes is plotted in the inset. (d) Variation of areal capacitance at different current densities. The inset shows the discharge/charge profiles obtained at different current densities from 0.5 to 20  $\text{mA cm}^{-2}$  (the current density is the applied current divided by the geometrical area of the electrode:  $0.785 \text{ cm}^2$ ). (e) Capacitance versus frequency. (f) Cycling tests measured at 1  $\text{mA cm}^{-2}$  for 10 000 cycles with the corresponding Coulombic efficiency.

shapes without any redox peaks, which represents the typical performance of electric double-layer capacitors (EDLCs) based on an electrostatic mechanism.<sup>2</sup> The EDLCs' behavior arises from the synergy between the carbon coating and the  $\text{Ta}_2\text{O}_5$  matrix. Additionally, the symmetrical shape of the cathodic and anodic sweeps in voltammograms recorded at different scan rates indicates reversible discharge/charge processes without side reactions. The voltammograms retain their rectangular or quasi-rectangular shape at fast scan rates up to 5  $\text{V s}^{-1}$ , whereas the voltammograms tend to tilt toward the vertical axis as a quasi-rectangle at 10  $\text{V s}^{-1}$ . This indicates that the heterogeneous nanotubes dominate the supercapacitive effect in their energy storage at scan rate up to 5  $\text{V s}^{-1}$  and show improved supercapacitive behavior over pristine  $\text{Ta}_2\text{O}_5$  NTs (Supporting

Information Figure S9a,b). It is common for areal capacitance ( $C_A$ ) to decrease when scan rates increase (Figure 4c) because the ion penetration and transport in and along the nanotubes requires sufficient time to generate higher capacitance. The  $C_A$  calculated from voltammograms at a scan rate of 10  $\text{mV s}^{-1}$  was 9.6  $\text{mF cm}^{-2}$ , and a  $C_A$  of 2.6  $\text{mF cm}^{-2}$  was obtained even at 10  $\text{V s}^{-1}$ . Therefore, the  $b$  values fitted from the log (peak current) versus log (scan rate) plot, as illustrated in the inset in Figure 4c, are 0.81 (cathodic) and 0.82 (anodic), which indicates a more surface-controlled (supercapacitive) electrode process.<sup>33</sup> Galvanostatic discharge/charge curves obtained at different current densities are presented in Figure 4d. The curves start from increased voltage drop ( $iR$  drop) as well as decreased discharge duration as the current density is

increased. The  $C_A$  (the inset in Figure 4d) decreased from  $18.2 \text{ mF cm}^{-2}$  at  $0.5 \text{ mA cm}^{-2}$  to  $8.4 \text{ mF cm}^{-2}$  at  $20 \text{ mA cm}^{-2}$ , which also indicates insufficient time for ion transportation into the interior of the nanotubes at high current densities. More likely, at a low rate ( $0.5 \text{ mA cm}^{-2}$ ), ion intercalation ( $\text{BF}_4^-$ ) and diffusion into the electrode is easier than at a high rate ( $20 \text{ mA cm}^{-2}$ ), which makes a difference in the capacitive behaviors at different rates. Full use of the active materials was not being achieved. It becomes more obvious that the  $C_A$  is greatly enhanced by forming a 3-D heterogeneous structure than in  $\text{T}_2\text{O}_5$  nanotubes alone (Supporting Information Figure S9c). Moreover, the Coulombic efficiency of the  $\text{T}_2\text{O}_5$  nanotubes is greatly enhanced from 67% to over 87% after coating with C- $\text{Fe}_2\text{O}_3$  NPs, which indicates a reduced internal resistance in the hybrid nanotubes. A strong frequency dependence of capacitance (Figure 4e) was apparent below 100 Hz, and a capacitance of 2.5 mF was obtained at 0.01 Hz. Similar frequency dependence trends were observed from  $C'$  and  $C''$  versus frequency curves (Supporting Information Figure S10), especially a peak frequency ( $f_p$ ) that appeared in the  $C''$  frequency curve, which was associated with the relaxation time constant ( $\tau_o$ ,  $\tau_o = 1/f_p$ ). Therefore,  $\tau_o$  is estimated to be 0.2 s for the heterogeneous nanotubes, which is even less than in multiwall carbon nanotubes (MWCNTs), indicating an excellent supercapacitive performance for the advanced electrode materials designed in this work.<sup>33</sup> Cycling tests (Figure 4f) measured at  $1 \text{ mA cm}^{-2}$  also indicate that the heterogeneous nanotubes provide stable capacitance over 10 000 cycles with less than 10% reduction. The Coulombic efficiency was maintained at over 90% during the cycling test.

Moreover, the heterogeneous nanotubes fabricated in this work deliver a specific capacitance up to  $18.2 \text{ mF cm}^{-2}$  based on the calculation from the discharge curve. The delivered capacitance in the hybrid nanotubes is higher than most state-of-the-art 3-D nanostructured thin-film supercapacitors (thin activated carbon films and vertically aligned multiwalled carbon nanotubes)<sup>34,35</sup> and carbon–metal oxides hybrid composites ( $\text{MnO}_2$  nanorods on reduced graphene oxide and conformal iron oxide on carbon).<sup>6,36,37</sup> Therefore, the 3-D heterogeneously hybrid nanotubes fabricated in this work deliver a bifunctional energy storage ability that embeds greatly enhanced LIBs and appealing supercapacitor performance into a single electrode.

## CONCLUSION

In summary, a 3-D heterogeneously nanostructured thin film was designed by uniformly anchoring carbon-onion-coated  $\text{Fe}_2\text{O}_3$  nanoparticles along  $\text{Ta}_2\text{O}_5$  NTs.  $\text{Ta}_2\text{O}_5$  NTs form a stable 3-D framework to support C- $\text{Fe}_2\text{O}_3$  NPs without agglomeration, while carbon onion layers play an important role in enhancing the conductivity of the electrode. The space-charge layers formed at the phase boundaries also provide opportunities for additional energy storage by charge separation. Such synergistic effect makes the 3-D heterogeneous nanostructured thin film deliver both excellent Li-ion battery (stabilized at  $800 \text{ mAh cm}^{-3}$ ) and supercapacitor (up to  $18.2 \text{ mF cm}^{-2}$ ) performances. By this approach, both Li-ion batteries and supercapacitors are successfully combined into the same electrode, which is promising for next generation hybrid energy storage and delivery devices.

## EXPERIMENTAL SECTION

**Fabrication.** Tantalum foils (0.05 mm, 99.9%, Sigma-Aldrich) were sonicated in ethanol (99.98%) for 1 h before being used as substrates.  $\text{Ta}_2\text{O}_5$  nanotubes were anodically grown in a solution of sulfuric acid (95.0–98.0%, Sigma-Aldrich) with 1 vol % HF (49%, Fisher Scientific) and 4 vol %  $\text{H}_2\text{O}$  at 50 V for 20 min. Experiments were carried out at room temperature in a two-electrode setup with platinum gauze as a counter electrode. After anodization, the samples were rinsed with  $\text{H}_2\text{O}$  followed by annealing at  $750^\circ\text{C}$  for 30 min in Ar. To deposit iron oxides into the  $\text{Ta}_2\text{O}_5$  nanotubes, 150 mg of iron(III) acetylacetonate (99.9%, Sigma-Aldrich) was dissolved in 10 mg of 2-pyrrolidinone (99%, Sigma-Aldrich) in a three-neck flask with stirring and nitrogen bubbling. Then,  $\text{Ta}_2\text{O}_5$  nanotubes on substrates were suspended in the solution by copper wire to avoid crushing the samples during stirring, and the flask was heated at reflux for 30 min under nitrogen. Afterward, the samples were washed several times with acetone and dried in a vacuum oven at  $60^\circ\text{C}$  for 2 h. For *in situ* CVD growth of carbon onions from the deposited iron oxides, the samples were reduced at  $550^\circ\text{C}$  in Ar (100 sccm) and  $\text{H}_2$  (100 sccm) for 10 min, and then carbon onions were formed at  $850^\circ\text{C}$  in  $\text{CH}_4$  (60 sccm) for 10 min. To convert metallic iron back to  $\text{Fe}_2\text{O}_3$ , the samples were postannealed at  $300^\circ\text{C}$  for 3 h in air.

**Characterization.** A JEOL 6500F SEM was used to investigate the morphology of the samples. A JEOL 2010 HRTEM was used

to observe the morphologies and lattice fringes of the samples. The crystal structure of the sample was evaluated using XRD analysis that was performed by a Rigaku D/Max Ultima II (Rigaku Corporation, Japan) configured with a Cu K $\alpha$  radiation, graphite monochromator, and scintillation counter. Investigation of the chemical composition of the anodic layers was performed using XPS (PHI Quantera XPS, Physical Electronics, USA).

**Electrochemical Measurement.** The heterogeneous nanotubes on tantalum foils were directly used as the working electrode without added binder, current collector, and conducting carbon as additives. The geometrical area of the electrode was  $1 \text{ cm}$  in diameter (about  $0.785 \text{ cm}^2$ ). The typical thickness of the electrode was  $3.5 \mu\text{m}$  with an apparent electrode density of  $5.1 \text{ g cm}^{-3}$ . Coin cells (CR2032, MTI Corporation, USA) were assembled in an argon-filled glovebox (VAC NEXUS, USA) with both moisture and oxygen content  $<1.5 \text{ ppm}$  and by using Li-metal foil (0.38 mm thick; 99.9%, Sigma-Aldrich, USA) as both the counter and reference electrodes, 1 M  $\text{LiPF}_6$  in ethylene carbonate (EC), dimethyl carbonate (DMC), diethyl carbonate (DEC) (1:1:1 vol %, MTI Corporation, USA) as the electrolyte, and polypropylene foil (Celgard, USA) as the separator. Afterward, the cells were left in ambient conditions at room temperature for 12 h to allow the porous electrode to become fully infiltrated by the electrolyte before the electrochemical measurements. The discharge/charge cycling tests were performed on a multi-channel battery analyzer (BST8-WA, MTI Corporation, USA).



The CV and EIS measurements were carried out with an electrochemical analyzer (CHI 608D, CH Instruments, USA). The voltammograms were measured in a potential window from 0.01 to 3 V (vs Li/Li<sup>+</sup>), and the EIS was carried out on the fresh cells at open circuit potentials with a frequency range of 10<sup>-2</sup> to 10<sup>5</sup> Hz with an ac signal amplitude of 5 mV. To investigate the electrode kinetics of the samples, the EIS was also carried out at different potentials (0.01, 0.5, 1.5, 2.5, and 3 V) during discharge/charge cycling. The impedance data were simulated by Z-view software (version 2.2, Scribner Associates, USA) to obtain the fitted Nyquist plots and simulated values for each equivalent circuit element. Symmetrical supercapacitors performance was tested in two-electrode configuration by assembling two pieces of the heterogeneous nanotubes on substrates into coin cell supercapacitors. Electrolyte was prepared by using 1 M tetraethylammonium tetrafluoroborate (TEA BF<sub>4</sub>, ≥99%, Sigma-Aldrich) in acetonitrile (≥99.5%, Fisher Scientific). Voltammograms were measured from 10 mV s<sup>-1</sup> to 10 V s<sup>-1</sup> in a potential range from 0 to 2.5 V. EIS was carried out on the fresh cells at open circuit potentials with a frequency range of 10<sup>-2</sup> to 10<sup>4</sup> Hz with an ac signal amplitude of 5 mV.

**Conflict of Interest:** The authors declare no competing financial interest.

**Acknowledgment.** We thank the Peter M. and Ruth L. Nicholas Post-Doctoral Fellowship of the Smalley Institute for Nanoscale Science and Technology for financial support (Y.Y.). Additional funding was provided by the ONR MURI Program (00006766, N00014-09-1-1066), AFOSR MURI program (FA9550-12-1-0035) and AFOSR (FA9550-09-1-0581).

**Supporting Information Available:** Supplementary figures. This material is available free of charge via the Internet at <http://pubs.acs.org>.

## REFERENCES AND NOTES

- Chan, C. K.; Peng, H.; Liu, G.; McIlwrath, K.; Zhang, X. F.; Huggins, R. A.; Cui, Y. High-Performance Lithium Battery Anodes Using Silicon Nanowires. *Nat. Nanotechnol.* **2008**, *3*, 31–35.
- Simon, P.; Gogotsi, Y. Materials for Electrochemical Capacitors. *Nat. Mater.* **2008**, *7*, 845–854.
- Tarascon, J.-M.; Armand, M. Issues and Challenges Facing Rechargeable Lithium Batteries. *Nature* **2001**, *414*, 359–367.
- Simon, P.; Gogotsi, Y.; Dunn, B. Where Do Batteries End and Supercapacitors Begin? *Science* **2014**, *343*, 1210–1211.
- Yang, Y.; Li, L.; Fei, H.; Peng, Z.; Ruan, G.; Tour, J. M. Graphene Nanoribbon/V<sub>2</sub>O<sub>5</sub> Cathodes in Lithium-Ion Batteries. *ACS Appl. Mater. Interfaces* **2014**, 10.1021/am501969m.
- Augustyn, V.; Simon, P.; Dunn, B. Pseudocapacitive Oxide Materials for High-Rate Electrochemical Energy Storage. *Energy Environ. Sci.* **2014**, *7*, 1597–1614.
- Bruce, P. G.; Scrosati, B.; Tarascon, J.-M. Nanomaterials for Rechargeable Lithium Batteries. *Angew. Chem., Int. Ed.* **2008**, *47*, 2930–2946.
- Chen, J. S.; Zhu, T.; Yang, X. H.; Yang, H. G.; Lou, X. W. Top-Down Fabrication of α-Fe<sub>2</sub>O<sub>3</sub> Single-Crystal Nanodisks and Microparticles with Tunable Porosity for Largely Improved Lithium Storage Properties. *J. Am. Chem. Soc.* **2010**, *132*, 13162–13164.
- Chen, J.; Xu, L.; Li, W.; Gou, X. α-Fe<sub>2</sub>O<sub>3</sub> Nanotubes in Gas Sensor and Lithium-Ion Battery Applications. *Adv. Mater.* **2005**, *17*, 582–586.
- Liu, C.; Li, F.; Lai-Peng, M.; Cheng, H.-M. Advanced Materials for Energy Storage. *Adv. Mater.* **2010**, *22*, E28–E62.
- Zhang, C.; Li, J.; Liu, E.; He, C.; Shi, C.; Du, X.; Hauge, R. H.; Zhao, N. Synthesis of Hollow Carbon Nano-onions and Their Use for Electrochemical Hydrogen Storage. *Carbon* **2012**, *50*, 3513–3521.
- Zhou, J.; Song, H.; Chen, X.; Zhi, L.; Yang, S.; Huo, J.; Yang, W. Carbon-Encapsulated Metal Oxide Hollow Nanoparticles and Metal Oxide Hollow Nanoparticles: A General Synthesis Strategy and Its Application to Lithium-Ion Batteries. *Chem. Mater.* **2009**, *21*, 2935–2940.
- Lee, K. T.; Jung, Y. S.; Oh, S. M. Synthesis of Tin-Encapsulated Spherical Hollow Carbon for Anode Material in Lithium Secondary Batteries. *J. Am. Chem. Soc.* **2003**, *125*, 5652–5653.
- Long, J. W.; Dunn, B.; Rolison, D. R.; White, H. S. Three-Dimensional Battery Architectures. *Chem. Rev.* **2004**, *104*, 4463–4492.
- Goodenough, J. B.; Kim, Y. Challenges for Rechargeable Li Batteries. *Chem. Mater.* **2010**, *22*, 587–603.
- Hu, C.-C.; Chang, K.-H.; Lin, M.-C.; Wu, Y.-T. Design and Tailoring of the Nanotubular Arrayed Architecture of Hydrous RuO<sub>2</sub> for Next Generation Supercapacitors. *Nano Lett.* **2006**, *6*, 2690–2695.
- Ban, C.; Wu, Z.; Gillaspie, D. T.; Chen, L.; Yan, F.; Blackburn, J. L.; Dillon, A. C. Nanostructured Fe<sub>3</sub>O<sub>4</sub>/SWNT Electrode: Binder-Free and High-Rate Li-Ion Anode. *Adv. Mater.* **2010**, *22*, E145–E149.
- Armand, M.; Tarascon, J.-M. Building Better Batteries. *Nature* **2008**, *451*, 652–657.
- Wen, Z.; Wang, Q.; Zhang, Q.; Li, J. *In Situ* Growth of Mesoporous SnO<sub>2</sub> on Multiwalled Carbon Nanotubes: A Novel Composite with Porous-Tube Structure as Anode for Lithium Batteries. *Adv. Funct. Mater.* **2007**, *17*, 2772–2778.
- Chang, J. P.; Steigerwald, M. L.; Fleming, R. M.; Opila, R. L.; Alers, G. B. Thermal Stability of Ta<sub>2</sub>O<sub>5</sub> in Metal-Oxide-Metal Capacitor Structures. *Appl. Phys. Lett.* **1999**, *74*, 3705.
- Ahn, H.-J.; Shim, H.-S.; Kim, Y.-S.; Kim, C.-Y.; Seong, T.-Y. Synthesis and Characterization of NiO-Ta<sub>2</sub>O<sub>5</sub> Nanocomposite Electrode for Electrochromic Devices. *Electrochem. Commun.* **2005**, *7*, 567–571.
- Zhang, H.; Yu, X.; Braun, P. V. Three-Dimensional Bicontinuous Ultrafast-Charge and -Discharge Bulk Battery Electrodes. *Nat. Nanotechnol.* **2011**, *6*, 277–281.
- Hu, X.; Yu, J. C.; Gong, J.; Li, Q.; Li, G. α-Fe<sub>2</sub>O<sub>3</sub> Nanorings Prepared by a Microwave-Assisted Hydrothermal Process and Their Sensing Properties. *Adv. Mater.* **2007**, *19*, 2324–2329.
- Kerrec, O.; Devilliers, D.; Groult, H.; Marcus, P. Study of Dry and Electrogenated Ta<sub>2</sub>O<sub>5</sub> and Ta/Ta<sub>2</sub>O<sub>5</sub>/Pt Structures by XPS. *Mater. Sci. Eng., B* **1998**, *B55*, 134–142.
- Kosynkin, D. V.; Higginbotham, A. L.; Sinitskii, A.; Lomeda, J. R.; Dimiev, A.; Price, B. K.; Tour, J. M. Longitudinal Unzipping of Carbon Nanotubes To Form Graphene Nanoribbons. *Nature* **2009**, *458*, 872–876.
- Reddy, M. V.; Yu, T.; Sow, C.-H.; Shen, Z. X.; Lim, C. T.; Rao, G. V. S.; Chowdari, B. V. R. α-Fe<sub>2</sub>O<sub>3</sub> Nanoflakes as an Anode Material for Li-Ion Batteries. *Adv. Funct. Mater.* **2007**, *17*, 2792–2799.
- Fu, Z.-W.; Huang, F.; Chu, Y.-Q.; Zhang, Y.; Qin, Q.-Z. Characterization of Amorphous Ta<sub>2</sub>O<sub>5</sub> Film as a Novel Anode Material. *J. Electrochem. Soc.* **2003**, *150*, A776–A782.
- Gowda, S. R.; Reddy, A. L. M.; Zhan, X.; Jafry, H. R.; Ajayan, P. M. 3D Nanoporous Nanowire Current Collectors for Thin Film Microbatteries. *Nano Lett.* **2012**, *12*, 1198–1202.
- He, Y.; Yu, X.; Wang, Y.; Li, H.; Huang, X. Alumina-Coated Patterned Amorphous Silicon as the Anode for a Lithium-Ion Battery with High Coulombic Efficiency. *Adv. Mater.* **2011**, *42*, 4938–4941.
- Nagasubramanian, G.; Doughty, D. H. Electrical Characterization of All-Solid-State Thin Film Batteries. *J. Power Sources* **2004**, *136*, 395–400.
- Kaskhedikar, N. A.; Maier, J. Lithium Storage in Carbon Nanostructures. *Adv. Mater.* **2009**, *21*, 2664–2680.
- Li, H. B.; Yu, M. H.; Wang, F. X.; Liu, P.; Liang, Y.; Xiao, J.; Wang, C. X.; Tong, Y. X.; Yang, G. W. Amorphous Nickel Hydroxide Nanospheres with Ultrahigh Capacitance and Energy Density as Electrochemical Pseudocapacitor Materials. *Nat. Commun.* **2013**, *4*, 1894.
- Portet, C.; Taberna, P. L.; Simon, P.; Flahaut, E. Influence of Carbon Nanotubes Addition on Carbon–Carbon Supercapacitor Performances in Organic Electrolyte. *J. Power Sources* **2005**, *139*, 371–378.
- Wei, L.; Nitta, N.; Yushin, G. Lithographically Patterned Thin Activated Carbon Films as a New Technology Platform for On-Chip Devices. *ACS Nano* **2013**, *7*, 6498–6506.

35. Béguin, F.; Presser, V.; Balducci, A.; Frackowiak, E. Carbons and Electrolytes for Advanced Supercapacitors. *Adv. Mater.* **2014**, *26*, 2219–2251.
36. Perera, S. D.; Rudolph, M.; Mariano, R. G.; Nijem, N.; Ferraris, J. P.; Chabal, Y. J.; Balkus, K. J., Jr. Manganese Oxide Nanorod-Graphene/Vanadium Oxide Nanowire-Graphene Binder-Free Paper Electrodes for Metal Oxide Hybrid Supercapacitors. *Nano Energy* **2013**, *2*, 966–975.
37. Sassin, M. B.; Mansour, A. N.; Pettigrew, K. A.; Rolison, D. R.; Long, J. W. Electroless Deposition of Conformal Nanoscale Iron Oxide on Carbon Nanoarchitectures for Electrochemical Charge Storage. *ACS Nano* **2010**, *4*, 4505–4514.